

GSA Data Repository 2020054

Dry sediment loading of headwater channels fuels post-wildfire debris flows in bedrock landscapes

Roman A. DiBiase^{1*}, Michael P. Lamb²

¹*Department of Geosciences, Pennsylvania State University, University Park, Pennsylvania 16802, USA.*

²*Division of Geological and Planetary Sciences, California Institute of Technology, Pasadena, California 91125, USA.*

*E-mail: rdibiase@psu.edu

Contents

Supplementary methods: Additional methodological details.

Supplementary table:

Table DR1. Airborne lidar dataset properties.

Supplementary figures:

Figure DR1. Hydrograph showing daily rainfall data from Big Tujunga Dam and mean daily runoff from Arroyo Seco.

Figure DR2. Comparison of network structure for areas experiencing dry ravel accumulation and subsequent erosion.

Figure DR3. Change resolved by differencing of September 2009 and 2015/2016 lidar datasets.

Figure DR4. Examples showing change between September 2009 and 2015/2016 lidar datasets.

Figure DR5. Map of difference Normalized Burn Ratio and location map for examples in Figs. DR3-4 and Figs. DR8-9.

Figure DR6. Comparison of predictions from 2D ravel routing model with topographic differencing of September 2009 and 2015/2016 lidar surveys.

Figure DR7. Maps showing fire history for study area prior to 2009 Station Fire.

Figure DR8. Pre-fire low-altitude oblique imagery of bedrock hillslopes north of the S. San Gabriel Fault Zone.

Figure DR9. Pre-fire low-altitude oblique imagery of bedrock hillslopes south of the S. San Gabriel Fault Zone.

Supplementary dataset S1: “Watersheds.zip” contains shapefiles of analyzed watersheds and watershed-averaged data.

References Cited

SUPPLEMENTARY METHODS

Airborne lidar point cloud differencing. To calculate topographic change, we used the Multiscale Model to Model Cloud Comparison (M3C2) point cloud change detection algorithm, which incorporates both dataset alignment uncertainty and the uncertainty associated with repeat sampling of rough surfaces (Lague et al., 2013). Analysis of point clouds maximizes spatially variable data resolution, avoids artifacts from gridding or interpolation procedures, and faithfully represents data gaps in the ground-classified point cloud.

The three airborne lidar datasets we analyzed were collected by different operators, with different instruments, and registered with different ground control (Table DR1), and thus preprocessing and alignment was required prior to change detection analysis. We projected the June 2009 and 2015/2016 lidar point clouds into the same coordinate system as the September 2009 dataset, which was the most robust of the three surveys due to the absence of vegetation following the 2009 Station Fire. To minimize systematic registration errors between the datasets, we divided the lidar point clouds into 3 km x 3 km tiles, and for each of the resulting tiles we aligned the ground-classified points of the June 2009 and 2015/2016 datasets to the ground-classified points of the September 2009 dataset using iterative closest point alignment as implemented in the software CloudCompare (version 2.10; <https://www.cloudcompare.org>). Last, we subsampled the ground-classified September 2009 point cloud to a minimum point spacing of 0.5 m to reduce computational costs and avoid bias in areas with high point density.

Using the M3C2 algorithm, we calculated the significant vertical topographic change between each ground point in the subsampled September 2009 dataset and the June 2009 and 2015/2016 ground-classified point clouds. We used a projection scale of 3.5 m to calculate surface change, which corresponds to the diameter of a cylindrical search window projected vertically from each point. This scale was chosen based on the smallest projection diameter for which 95% of the calculations include at least 4 data points from each point cloud, as recommended by Lague et al. (2013) to ensure robust roughness-based uncertainty estimates. For each point in the subsampled September 2009 point cloud, a mean vertical difference between the September 2009 point cloud and both the June 2009 and 2015/2016 point clouds was calculated over the scale of the projection window. To determine whether this change was significant or not, we calculated separately the slope-normal change compared to the slope-normal surface roughness using the M3C2 algorithm, including an additional registration error of 20 cm that incorporates positional uncertainty and range uncertainty at each point (~5–30 cm; Table DR1). Each point in the subsampled September 2009 point cloud was thus assigned one of three potential values: the mean vertical elevation change if the change was significant; “0” if change was not significant; or “no data” if there were no data points sampled from the compared dataset within the 3.5 m diameter projection window.

Although the resulting point clouds of significant change detection most faithfully represent the variable data coverage for each lidar survey, calculating catchment-scale sediment budgets is most straightforward using regularized grids. Thus, we rasterized each point cloud of significant change (June 2009–September 2009 and September 2009–2015/2016) using a grid size of 1 m. A scale of 1 m was chosen to best preserve the spatial resolution of the change detection map while minimizing data gaps in the area burned by the Station Fire. For unburned areas, vegetation cover limits the density of ground-classified points in some places to less than 1 pt m⁻², resulting in more data gaps. Inspection of the 1 m resolution change detection raster suggests that this resolution is sufficient to characterize spatial patterns of change in areas with

high ground-classified point density (>2 pts m^{-2}). We see evidence of channel fill, erosion, roadwork, reservoir fill, and landslides that are well-resolved through comparison of gridded slope and hillshade maps (Figs. DR3–DR4). There is also noise associated with poor classification of dense vegetation on unburned hillslopes (Fig. DR4), which has the potential to bias spatially averaged estimates of erosion or deposition. To limit the effect of this noise on hillslopes and focus on change detection in channels, we filtered the change detection data using a 15 m wide buffer along the channel network, which we defined using a threshold accumulation area of 1.25×10^3 m^2 (50 pixels in a 5 m digital elevation model used for calculating flow accumulation).

To visualize large-scale patterns in topographic change between September 2009 and 2015/2016, we delineated 397 headwater catchments ($0.1 - 2.0$ km^2) that are not affected by major roads or other anthropogenic disturbance, and calculated the average erosion, ε , according to:

$$\varepsilon = \frac{dx^2 \sum A_c \Delta z_{2009-2015}}{A}, \quad (1)$$

where dx is the raster grid size (1 m), A is the total catchment area, and $\Delta z_{2009-2015}$ is the vertical change from September 2009 to 2015/2016, which is summed over the area within the channel buffer, A_c . As an assessment of how robust this estimate of catchment erosion is, we calculated the fraction of “no data” pixels within the channel buffer area, f_c , defined by:

$$f_c = \frac{A_c - ndx^2}{A_c}, \quad (2)$$

where n is the number of “no data” pixels within the channel buffer area, A_c . The degree of data coverage along channel networks is higher for burned catchments due to higher density of ground return points. For unburned regions (difference Normalized Burn Ratio $dNBR < 0.1$), the mean value of f_c is 0.6. For burned catchments ($dNBR > 0.1$) the mean value of f_c is 0.9. We highlight in Fig. 1 areas where $f_c < 0.8$ to indicate greater uncertainty in catchment volume estimates here. We assume that overall channels are being eroded, with minimal redeposition in the headwater catchments we analyze. Thus, we interpret our reported erosion values as conservative estimates of channel erosion.

Slope calculation. We calculated the local slope across our study area using the dip of a plane fit to all points within a 15 m diameter window around each point in a 3 m-resampled ground-classified point cloud of the 2015/2016 lidar dataset. The resulting values were then rasterized to a 3 m grid, and the mean slope was calculated for each analyzed catchment. We used the 2015/2016 dataset for this calculation to minimize the effect of low-sloping channel fills prevalent in the September 2009 lidar data.

Burn severity metric calculation. We estimated burn severity using the difference Normalized Burn Ratio ($dNBR$) calculated from Landsat 5 scenes taken before and after the Station Fire (August 6, 2009 and November 26, 2009). We calculated $dNBR$ using band 4 (NIR , 0.77–0.90 μm wavelength) and band 7 ($SWIR$, 2.08–2.35 μm wavelength), according to:

$$dNBR = \left(\frac{NIR-SWIR}{NIR+SWIR} \right)_{prefire} - \left(\frac{NIR-SWIR}{NIR+SWIR} \right)_{postfire}. \quad (3)$$

For each analyzed catchment we calculated the mean value of $dNBR$, defining areas with $dNBR < 0.1$ as “unburned” and areas with $dNBR > 0.1$ as “burned” (Key and Benson, 2006).

Debris basin data. We used debris volume data from water years 2010 and 2011 (Los Angeles County Department of Public Works, 2011; 2012a) to independently compare total observed sediment yields to our catchment erosion estimates based on topographic differencing of the September 2009 and 2015/2016 lidar data. For each of 20 burned watersheds containing a debris basin at their outlet, we divided the reported debris volumes by the upstream contributing area to determine debris basin sediment yield (Fig. 1 and Fig. 3A), which often encompasses multiple individual debris flow events (Kean et al., 2011). We assumed for simplicity no change in density between eroded channel deposits and material accumulated in debris basins and that all debris basin volumes are accurate reflections of the total mass export. We assigned uncertainty to these estimates based on the reported practice of clearing unburned debris basins once they reach 25% of their capacity and recently (past 5 years) burned debris basins once they reach 5% of their capacity (Los Angeles County Department of Public Works, 2012b). Thus, we assumed that all basins were less than 25% full prior to the 2009 Station Fire, and less than 5% full in fall 2014. Based on analysis of rainfall and runoff data highlighting the severe drought conditions from 2012-2016 (Fig. DR1), we assumed that minimal erosion or deposition occurred between fall 2014 and the time of the 2015/2016 lidar flights.

Vegetation storage model. We used a vegetation storage model calibrated to the San Gabriel Mountains (DiBiase and Lamb, 2013; Lamb et al., 2013) to estimate the potential dry ravel storage capacity for each catchment prior to the 2009 Station Fire. Based on laboratory tilt-table experiments, the volume of sediment stored behind vegetation per unit area, V , is characterized by:

$$V = C \frac{W^3}{24} \frac{S_r^2}{0.9 \left(\frac{S-S_f}{S_f} \right)^{0.6}}, \quad (4)$$

where C is the vegetation areal density, W is plant width, S_r is the tangent of the angle of repose of sediment, S_f is the (static) friction slope of sediment, and S is the local surface slope determined from lidar topography (Lamb et al., 2013). Following DiBiase and Lamb (2013) and Lamb et al. (2013), we assumed $C = 0.5$ plants/m², $W = 1$ m, $S_r = 0.76$, and $S_f = 0.58$. We assumed similar vegetation cover for all catchments analyzed, based on inspection of pre-fire aerial imagery (Figs. DR8 and DR9). In general, vegetation cover depends mainly on local topographic position and aspect, and does not systematically vary across the study area. Slopes less than 30° ($S < 0.58$) were assumed to have a stable continuous soil mantle and areas with slopes steeper than 45 degrees were assumed to be bare rock with sparse vegetation (DiBiase et al., 2012; DiBiase and Lamb, 2013). Mean volumetric storage per area was then calculated for each watershed draining to a monitored debris basin and plotted on Fig. 3A.

Ravel routing model. To predict landscape scale patterns of dry sediment loading, we used the 2D ravel-routing model of DiBiase et al. (2017), which is a particle-based model that routes sediment down lidar topography of steep hillslopes using a modified Coulomb friction law approximation for particle acceleration:

$$A = g(\sin \theta - \tan \varphi \cos \theta) - \kappa|V|, \quad (5)$$

where A is downslope particle acceleration, V is particle velocity, g is gravitational acceleration, θ is the local topographic slope determined from lidar topography, φ is an effective (dynamic) friction angle between the particle and hillslope, and κ is a dimensional shock term coefficient that reflects momentum loss due to particle collisions. The effective friction slope, $\tan \varphi$, is a stochastic variable that depends on the relative roughness of the particle and the hillslope surface, such that:

$$\tan \varphi = \text{pdf}(\tan \mu) = \frac{1}{\tan \bar{\mu}} \exp\left(-\frac{\tan \mu}{\tan \bar{\mu}}\right), \quad (6)$$

where $\text{pdf}(\tan \mu)$ indicates an exponential probability distribution of the random variable $\tan \mu$ and $\tan \bar{\mu}$ is the mean effective friction slope.

Particle motion is initiated at a given cell with an initial downslope velocity V_0 , and is routed downslope with each model time step i via a series of “hops” until coming to rest:

$$V_{i+1} = V_i + A_i \Delta t, \quad (7)$$

where A is calculated according to Eqn. 5 above, and Δt is a timestep that scales with hop distance. The model is implemented by releasing particles and tracking their transport pathway and stopping locations, resulting in spatially distributed predictions of post-wildfire dry sediment accumulation for comparison with our lidar-derived topographic change detection measurements.

We implemented two scenarios of the 2D ravel routing model. In the first case, we assumed a uniform source for dry ravel (DiBiase et al., 2017). For the second case, we weighted the sources according to a vegetation storage model calibrated to pre-fire conditions in the San Gabriel Mountains (DiBiase and Lamb, 2013; Lamb et al., 2013), as described above. All other parameters were held equal and calibrated based on field experiments (DiBiase et al., 2017): $g = 9.8 \text{ m s}^{-2}$; $\tan \bar{\mu} = 0.5$; $\kappa = 1.4 \text{ m s}^{-1}$; $V_0 = 2 \text{ m s}^{-1}$; $\Delta t = 0.3 \text{ s}$. Because we found no significant difference in the pattern of sediment loading from the uniform and vegetation storage weighted models (Fig. DR6), we used the uniform source model for all other analysis.

To compare the results from our particle-based ravel routing model with our topographic differencing data, we focused on the network-scale pattern of sediment loading predicted by the model. This was accomplished qualitatively by comparing maps of modeled relative deposit thickness (Fig. 2B and Fig. DR6) or the distribution of modeled deposits thicker than a critical value (Fig. DR2). We quantified the network-scale deposition patterns by comparing the slope and drainage area of landscape pixels with modeled sediment accumulation thicker than a critical value (Fig. 2F and Fig. DR2).

Table DR1. Airborne lidar dataset properties.

	2009 Pre-fire lidar	2009 Post-fire lidar	2015/2016 lidar
Data Source	U.S. Geological Survey	National Center for Airborne Laser Mapping	Los Angeles County/ U.S. Geological Survey
Collection date range	June 2–June 22, 2009	September 29–October 1, 2009	September 2015–October 2016
Ground-classified point density	0.9–1.9 pts m ⁻² (mean 1.3 pts m ⁻²)	0.6–3.7 pts m ⁻² (mean 2.3 pts m ⁻²)	0.7–2.5 pts m ⁻² (mean 1.4 pts m ⁻²)
Positional uncertainty	0.06–0.2 m	0.05–0.3 m	Not provided
Original projection	NAD1983 UTM ZONE 11N [EPSG:26911]	NAD1983 UTM ZONE 11N [EPSG:26911]	CA State Plane V NAD83 [EPSG:2229]
Original vertical datum	NAVD88 Geoid 03 [EPSG:5703]	NAVD88 Geoid 03 [EPSG:5703]	NAVD88 Geoid 12B [EPSG:5103]

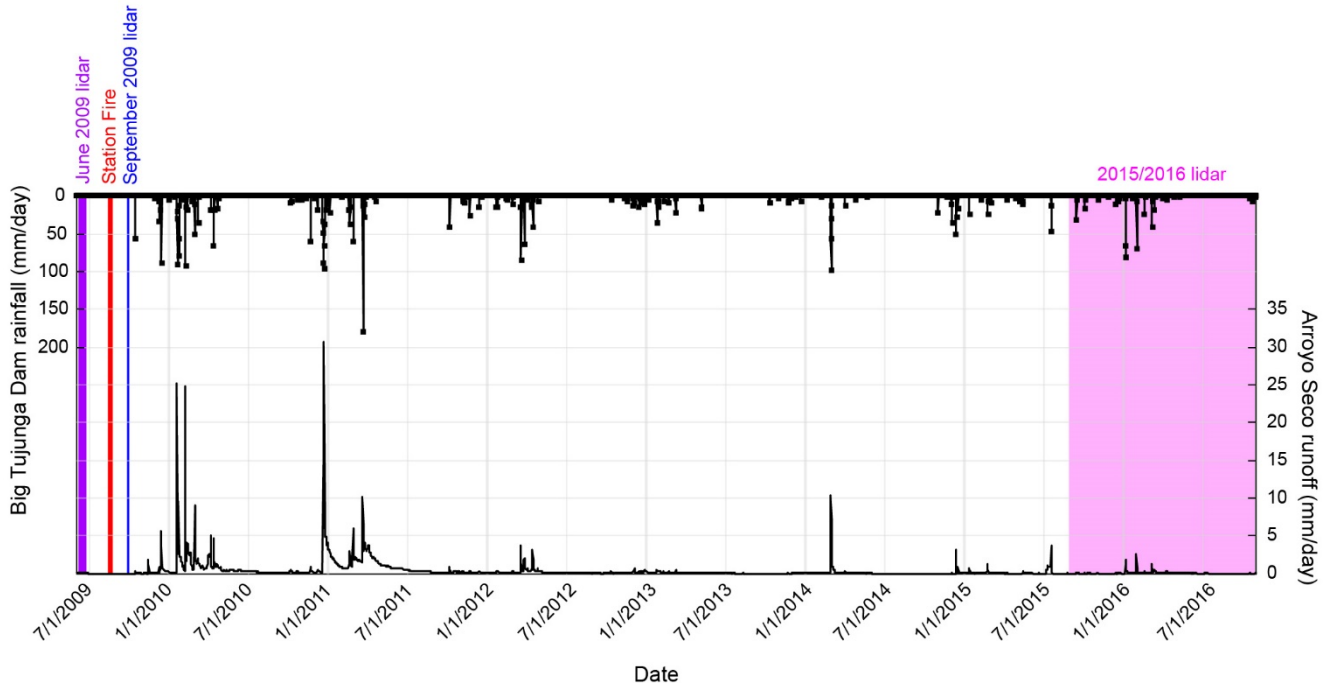


Figure DR1. Hydrograph showing daily rainfall data from Big Tujunga Dam (Los Angeles County Department of Public Works, 2011; 2012; 2013; 2014; 2015; 2016; 2017) and mean daily runoff from Arroyo Seco (USGS site 11098000). Vertical colored bars indicate dates of lidar surveys and main growth period of the 2009 Station Fire.

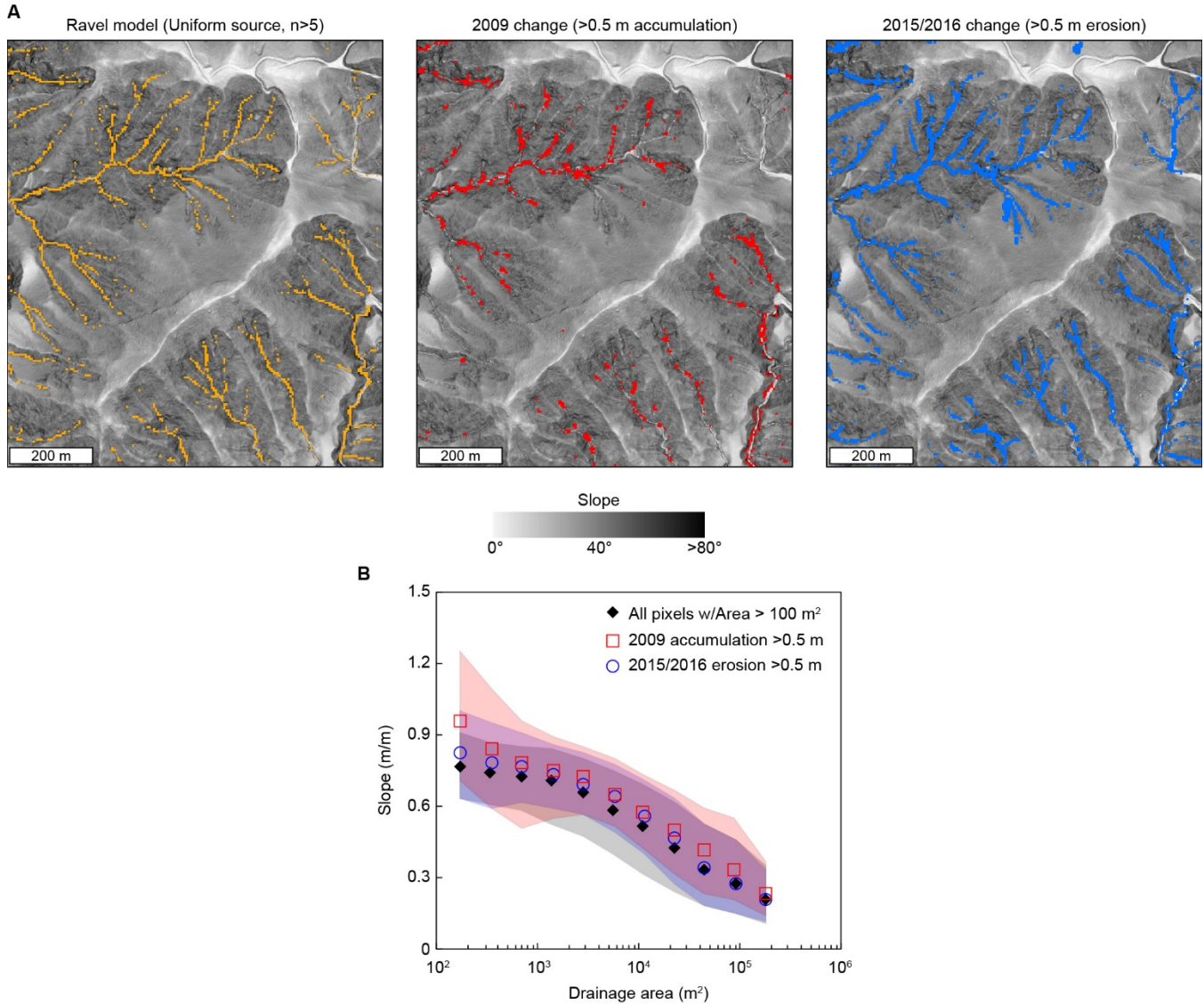


Figure DR2. Comparison of network structure for areas experiencing dry ravel accumulation and subsequent erosion. **A:** Slopeshade map of Brown Mountain region (Fig. DR3C), showing location of regions predicted to have high ravel deposition (orange, from Fig. DR6B); areas that showed accumulation of > 0.5 m of dry ravel based on differencing of June 2009 and September 2009 lidar datasets (red); and areas that showed > 0.5 m of erosion based on differencing of 2015/2016 and September 2009 lidar datasets (blue). **B:** Slope-area plots showing distribution of all pixels and areas experiencing dry sediment loading and subsequent erosion. Symbols correspond to median slope and shaded areas correspond to inner quartile range over logarithmic bins of drainage area.

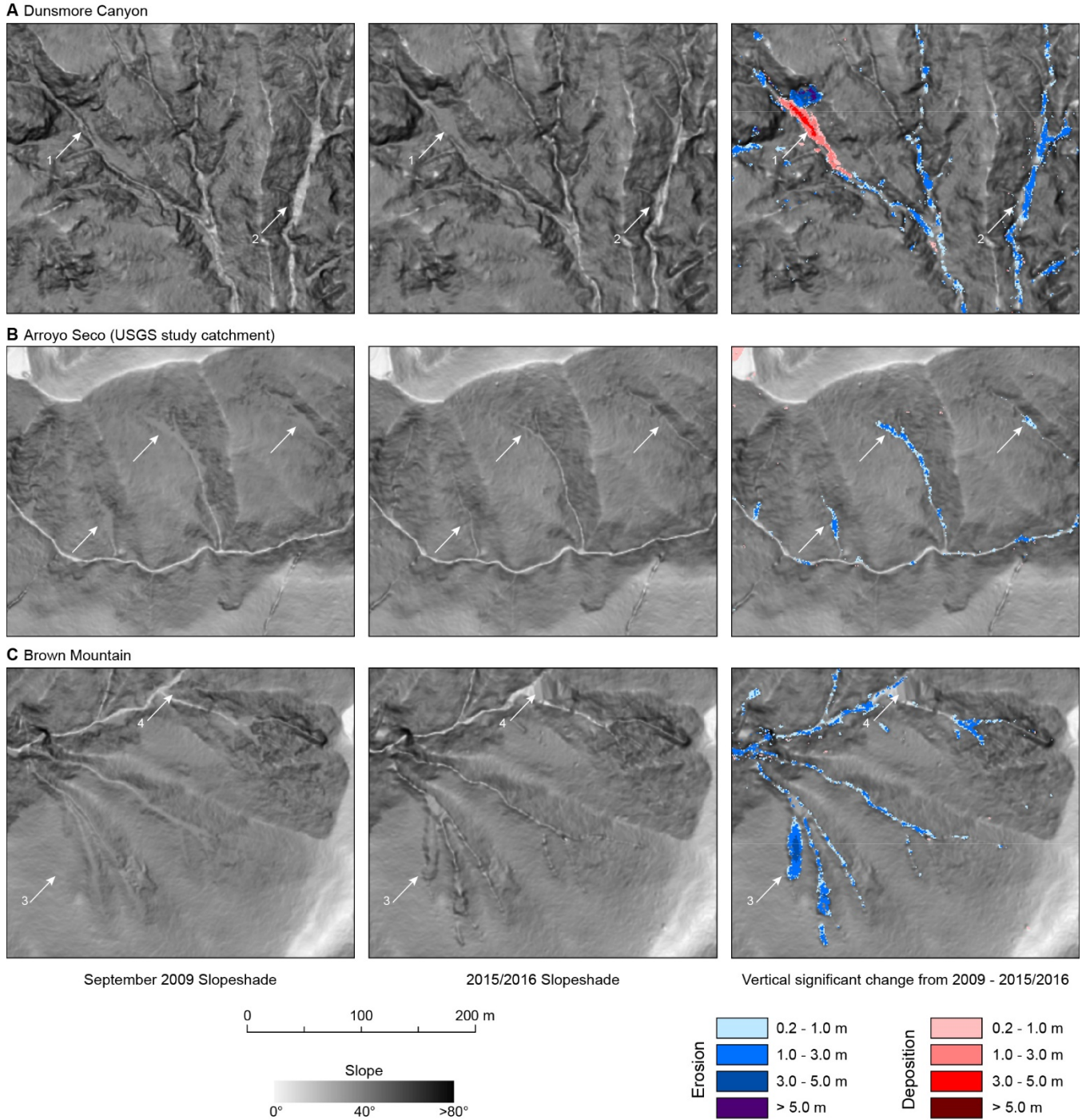


Figure DR3. Change resolved by differencing of September 2009 and 2015/2016 lidar datasets. **A:** Rockfall in Dunsmore canyon (arrow 1) and erosion of channel fill (arrow 2). **B:** Erosion of channel fill (arrows) in the USGS Arroyo Seco study catchment (Kean et al., 2011; Schmidt et al., 2011; Staley et al., 2014). **C:** Erosion of channel fill and erosion by headward retreat of shallow landslide (arrow 3). Gap in 2015/2016 lidar point cloud results in raster artifact (arrow 4) but does not propagate as significant change detection. Locations indicated in Fig. DR5.

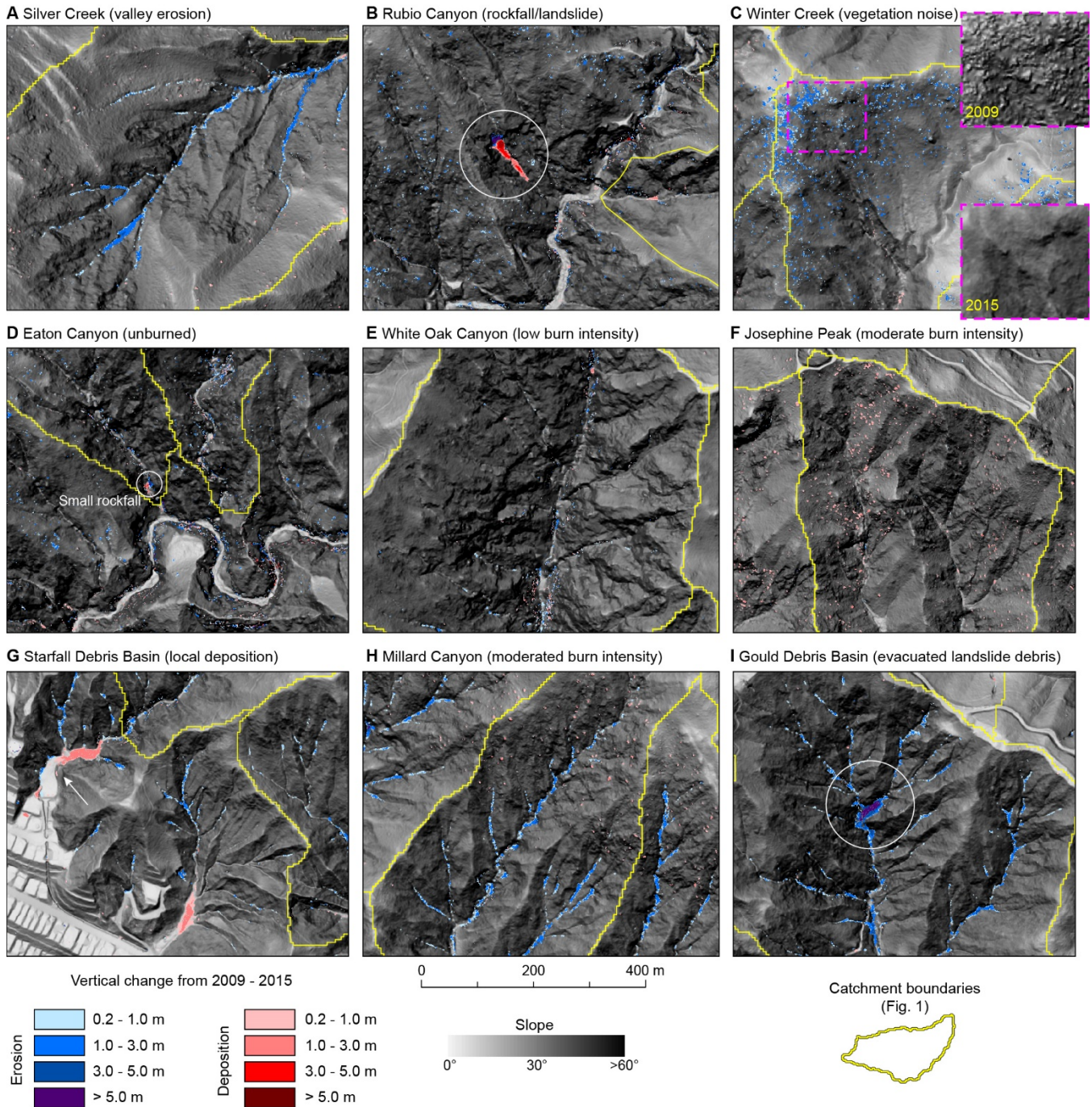


Figure DR4. Examples showing change between September 2009 and 2015/2016 lidar datasets. White circles and arrows highlight areas of interest indicated in panel headings. Dashed box in C indicates extent of inset panels comparing lidar vegetation filtering in unburned areas that leads to spurious topographic change. Locations indicated in Fig. DR5.

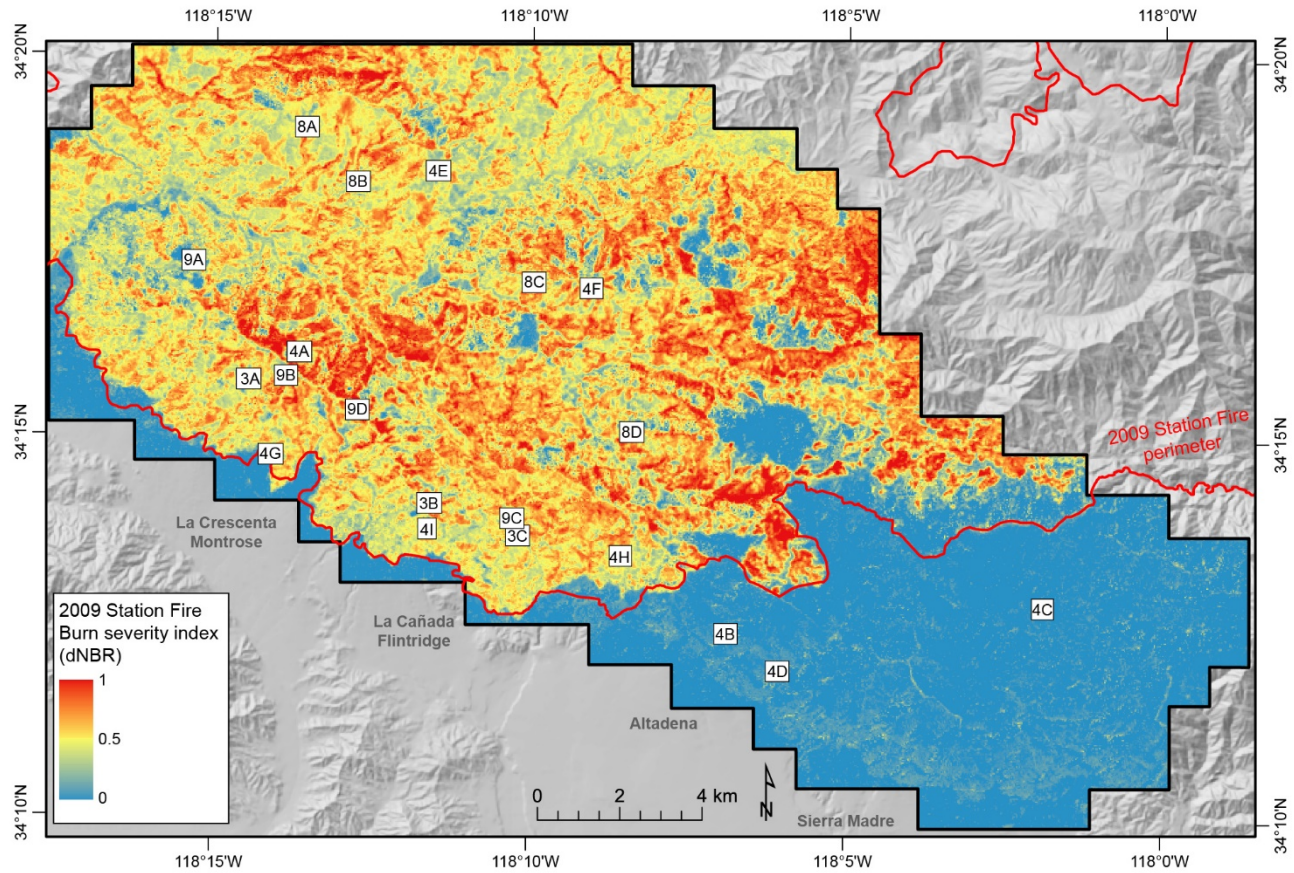


Figure DR5. Map of difference Normalized Burn Ratio (dNBR), a metric of burn severity, for 2009 Station Fire, showing location of examples highlighted in Fig. DR3 (3A–C), Fig. DR4 (4A–I), Fig. DR8 (8A–D), and Fig. DR9 (9A–D).

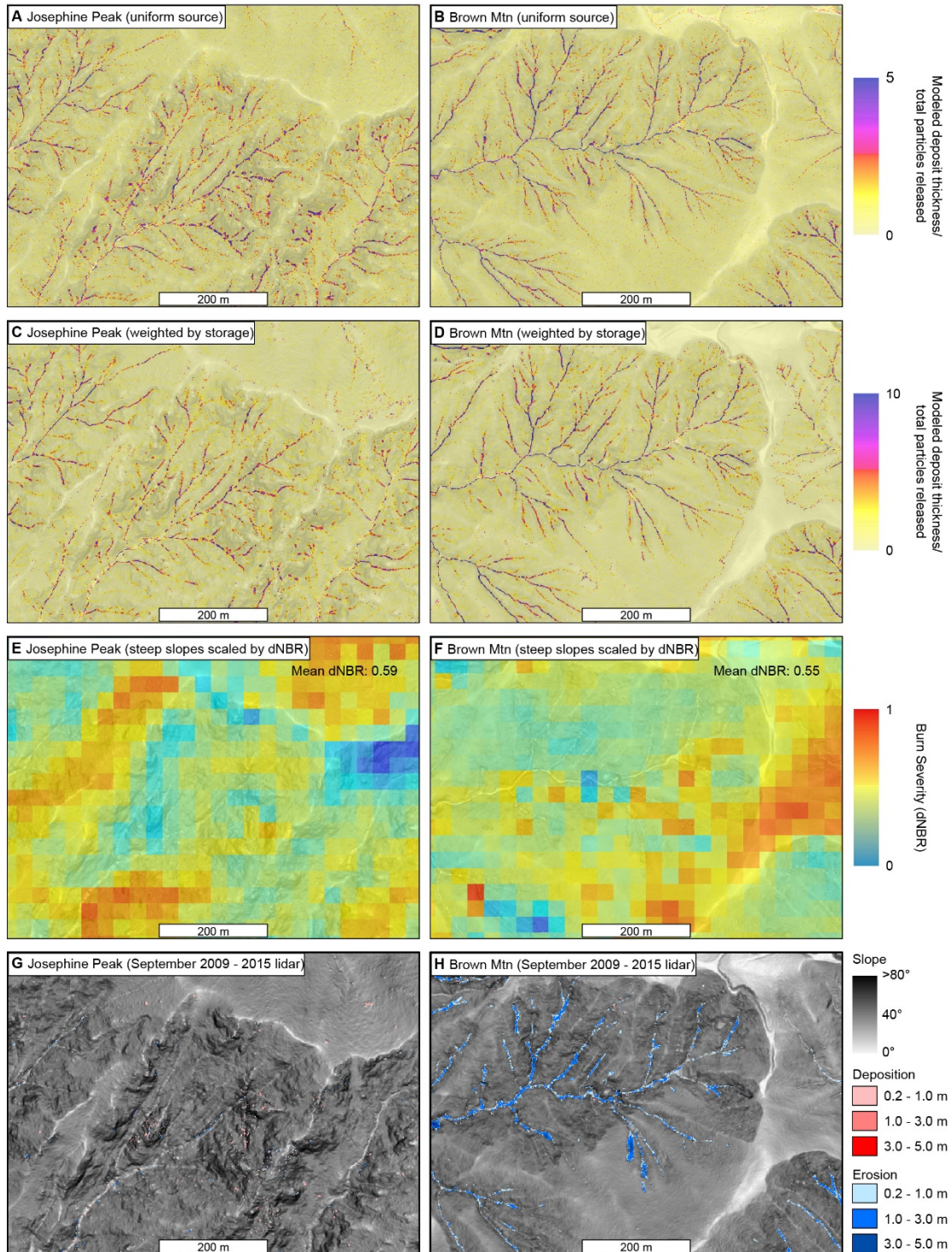


Figure DR6. Comparison of predictions from 2D ravel routing model (DiBiase et al., 2017) with topographic differencing of September 2009 and 2015/2016 lidar surveys near Josephine Peak (A, C, E, G; Fig. DR4F) and Brown Mountain (B, D, F, H; Fig. DR3C). Ravel model deposit thickness is normalized by average number of particles released per cell, which was done either uniformly at each cell (A, B) or weighted using a dry ravel storage model (C, D; DiBiase and Lamb, 2013; Lamb et al., 2013).

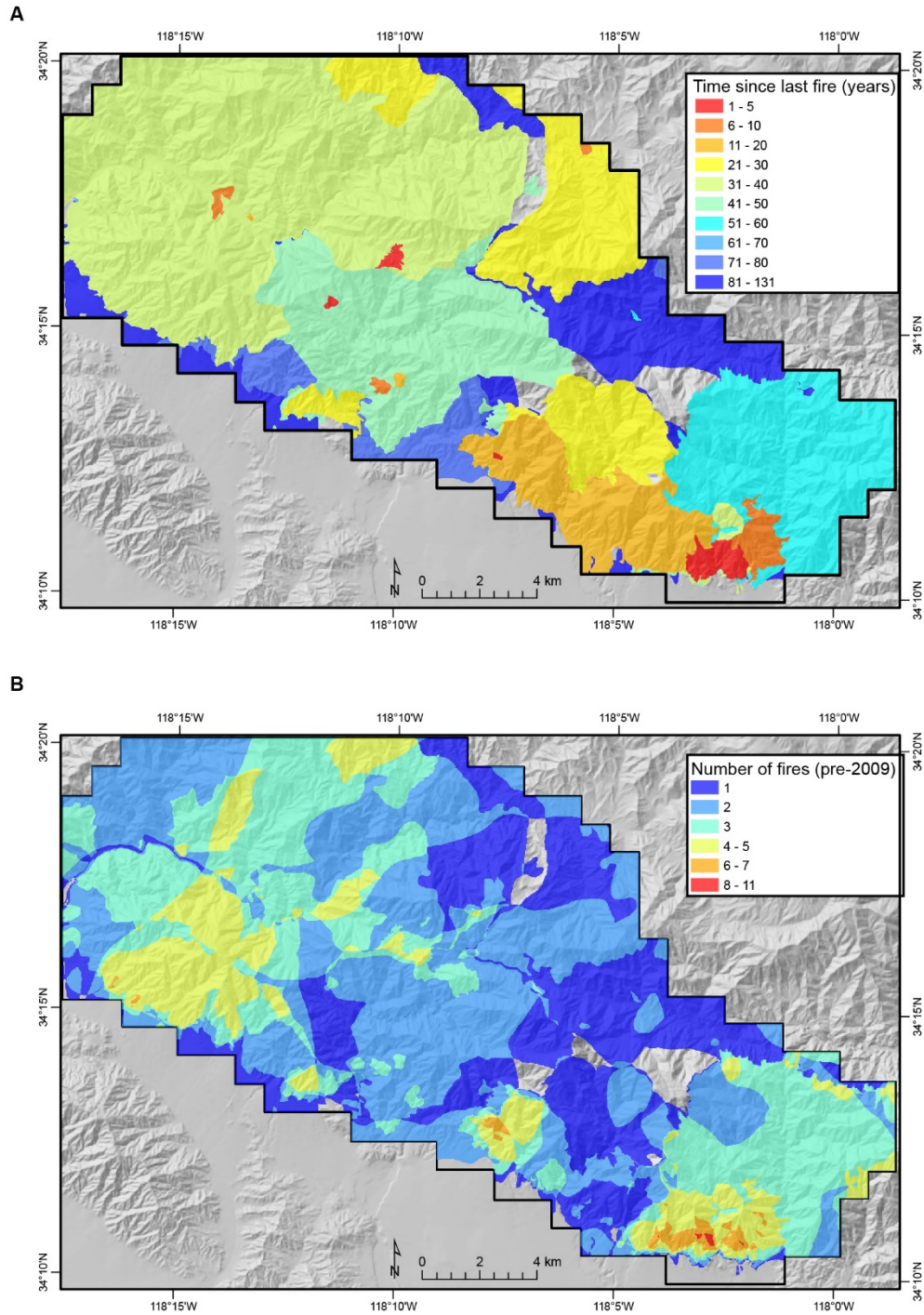


Figure DR7. Maps showing fire history for study area prior to 2009 Station Fire (California Department of Forestry and Fire Protection Historical Fire Perimeters, accessed July 9, 2019 from <https://frap.fire.ca.gov/mapping/gis-data/>). **A:** Number of years since last fire. **B:** Number of fires since 1878.

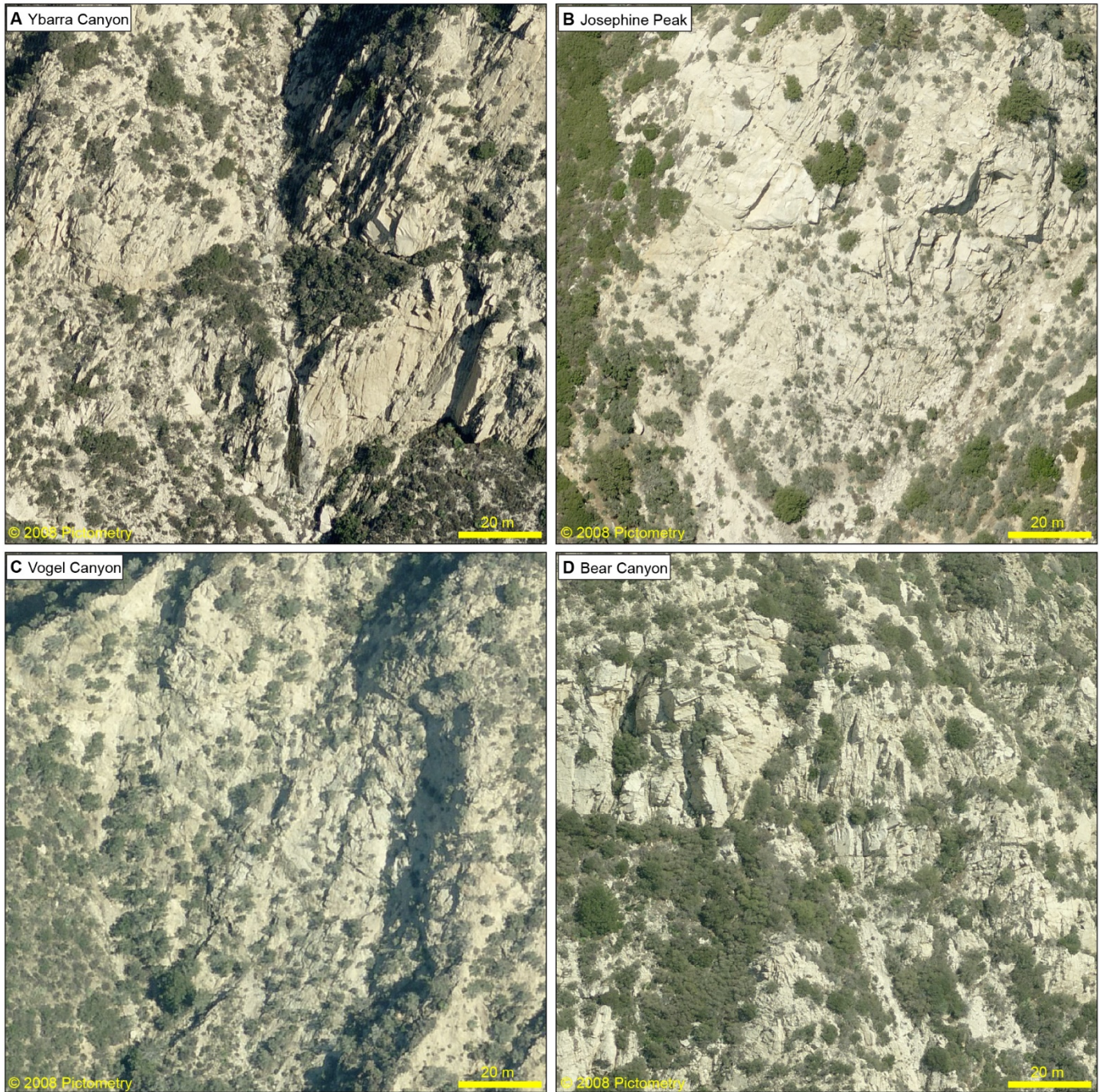


Figure DR8. Pre-fire (2008) low-altitude oblique imagery of bedrock hillslopes north of the S. San Gabriel Fault Zone, highlighting bedrock fracture patterns in steep cliffs composed of granodiorite bedrock (Kgrd, Trlgd) (Campbell et al., 2014). None of these burned sites experienced significant post-wildfire channel fill or subsequent erosion. Location of images shown in Fig. DR5. Images from Pictometry Corp.

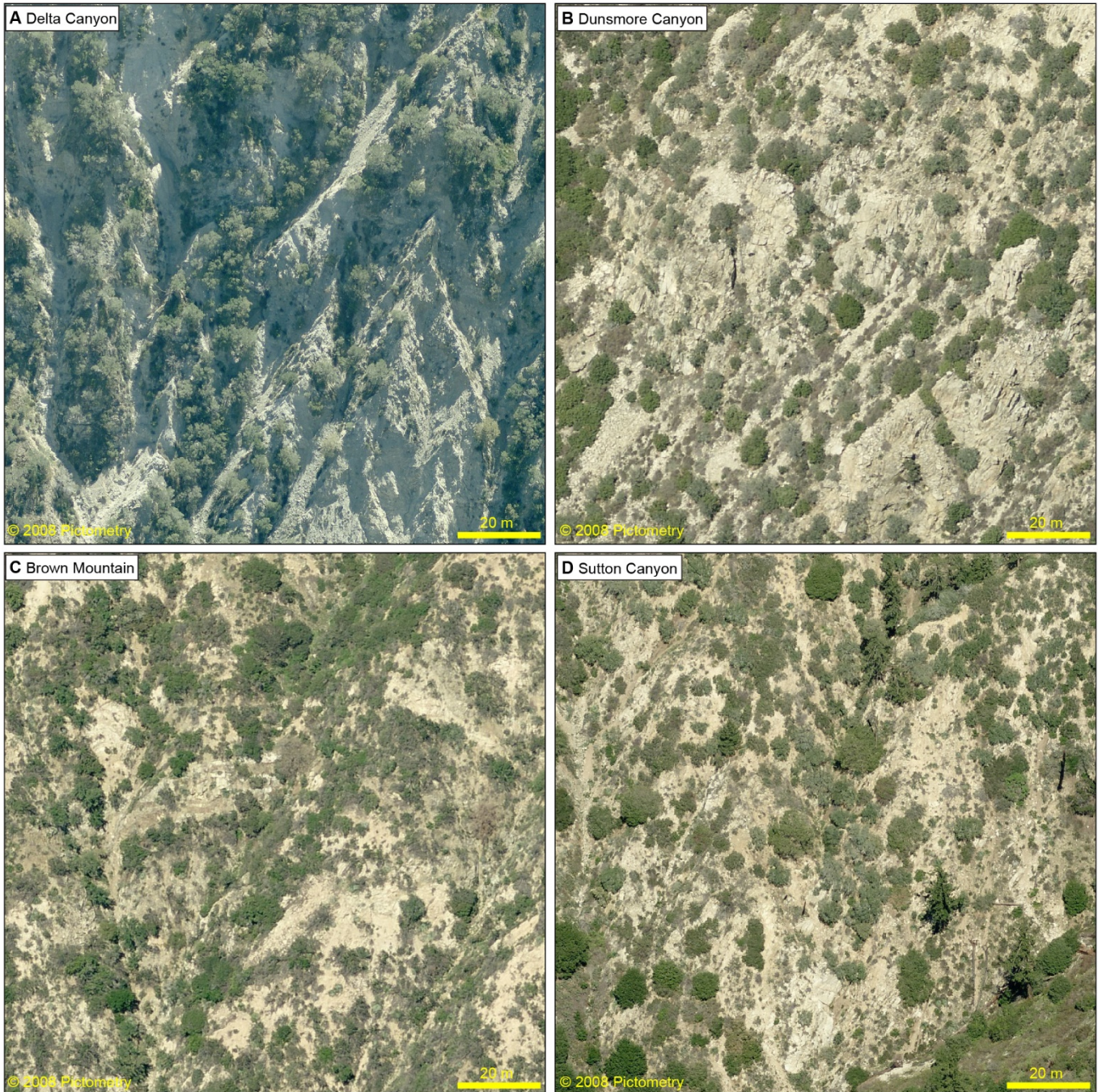


Figure DR9. Pre-fire (2008) Low-altitude oblique imagery of bedrock hillslopes south of the S. San Gabriel Fault Zone, highlighting biotite monzogranite bedrock (Mzmg)(Campbell et al., 2014) fractured near or below the resolution of the images (5-10 cm/pixel). All sites shown experienced both high post-fire dry sediment loading and high post-storm erosion. Locations shown in Fig. DR5. Images from Pictometry Corp.

REFERENCES CITED

- Key, C. H. and Benson, N. C., 2006, Landscape Assessment (LA) Sampling and Analysis Methods, in Lutes, D. C., Ed. FIREMON: Fire Effects Monitoring and Inventory System (Gen. Tech. Rep. RMRS-GRT-164-CD, USDA Forest Service).
- Lague, D., Brodu, N., and Leroux, J., 2013, Accurate 3D comparison of complex topography with terrestrial laser scanner: Application to the Rangitikei canyon (N-Z): ISPRS Journal of Photogrammetry and Remote Sensing, v. 82, p. 10-26, doi.10.1016/j.isprsjprs.2013.04.009.
- Los Angeles County Department of Public Works, 2012a, "Hydrologic Report 2010-2011", accessed July 9, 2019 from <http://www.ladpw.org/wrd/report/>.
- Los Angeles County Department of Public Works, 2012b, "Strategic Plan Section 4: Historical Sediment Deposition and Removal", accessed August 7, 2019 from <https://dpw.lacounty.gov/lacfd/sediment/stplan.aspx>.
- Los Angeles County Department of Public Works, 2013, "Hydrologic Report 2011-2012", accessed July 9, 2019 from <http://www.ladpw.org/wrd/report/>.
- Los Angeles County Department of Public Works, 2014, "Hydrologic Report 2012-2013", accessed July 9, 2019 from <http://www.ladpw.org/wrd/report/>.
- Los Angeles County Department of Public Works, 2015, "Hydrologic Report 2013-2014", accessed July 9, 2019 from <http://www.ladpw.org/wrd/report/>.
- Los Angeles County Department of Public Works, 2016, "Hydrologic Report 2014-2015", accessed July 9, 2019 from <http://www.ladpw.org/wrd/report/>.
- Los Angeles County Department of Public Works, 2017, "Hydrologic Report 2015-2016", accessed July 9, 2019 from <http://www.ladpw.org/wrd/report/>.